

Minimizing light exposure with the programmable array microscope

W. CAARLS*[†], B. RIEGER[‡], A.H.B. DE VRIES*,
D.J. ARNDT-JOVIN* & T.M. JOVIN*

*Laboratory of Cellular Dynamics, Max Planck Institute for Biophysical Chemistry, Göttingen, Germany

[†]Department of Biomechanical Engineering, Faculty of Mechanical, Maritime and Materials Engineering, Delft University of Technology, The Netherlands

[‡]Quantitative Imaging Group, Delft University of Technology, Delft, The Netherlands

Key words. Controlled light exposure microscopy, photobleaching, programmable array microscope, region of interest, segmentation, tracking.

Summary

The exposure of fluorophores to intense illumination in a microscope often results in photobleaching and phototoxicity, thus constituting a major limiting factor in time lapse live cell or single molecule imaging. Laser scanning confocal microscopes are particularly prone to this problem, inasmuch as they require high irradiances to compensate for the inherently low duty cycle of point scanning systems. In the attempt to maintain adequate speed and signal-to-noise ratios, the fluorophores are often driven into saturation, thereby generating a nonlinear response.

One approach for reducing photodegradation in the laser scanning confocal microscope is represented by controlled light exposure microscopy, introduced by Manders and colleagues. The strategy is to reduce the illumination intensity in both background areas (devoid of information) as well as in bright foreground regions, for which an adequate signal-to-noise ratio can be achieved with lower excitation levels than those required for the less intense foreground pixels/voxels. Such a variable illumination scheme can also be exploited in widefield microscopes that employ lower irradiance but higher illumination duty cycles. We report here on the adaptation of the controlled light exposure microscopy principle to the programmable array microscope, which achieves optical sectioning by use of a spatial light modulator (SLM) in an image plane as a programmable mask for illumination and conjugate (and nonconjugate) detection. By incorporating the basic controlled light exposure microscopy concept for minimizing exposure, we have obtained a reduction in the

rate of photobleaching of up to ~5-fold, while maintaining an image quality comparable to regular imaging with the programmable array microscope.

Introduction

Prolonged live cell imaging is an essential tool in the study of extra- or intracellular dynamics such as during differentiation-induced cell migration, signalling, exo/endo-cytosis and intracellular trafficking. Except for exceptionally photostable nanoparticle probes such as quantum dots (Bruchez *et al.*, 1998; Lidke & Arndt-Jovin 2004), the fluorophores used in these measurements exhibit photobleaching, thereby limiting the number of images that can be acquired and producing unwanted reactive oxygen species that can reduce the viability of the sample. A trade-off has to be made between temporal and/or spatial resolution, signal-to-noise ratio (SNR), and the observation time. It is therefore important to restrict the light dose to the minimum required for achieving a certain SNR. In this regard, widefield microscopes are generally preferable to point-scanning confocal instruments because they provide a good SNR even with low-power light sources such as light emitting diodes. However, optical sectioning based on conventional widefield illumination requires deconvolution of a through-focus series of images, a procedure that is ill-suited for real-time high-speed operation.

We have been engaged in the long-term development of a high-speed optically sectioning widefield imaging system [denoted the programmable array microscope (PAM)] based on structured illumination and conjugate detection implemented with an SLM located in a primary image plane (Verveer *et al.*, 1998). An inherent feature is the rapid, (re)programmable adjustment of local excitation intensity,

Correspondence to: T.M. Jovin, Laboratory of Cellular Dynamics, Max Planck Institute for Biophysical Chemistry, Am Faßberg 11, 37077 Göttingen, Germany. Tel: +49-551-201-1382; fax: +49-551-201-1467; e-mail: tjovin@gwdg.de

unavailable in spinning disk (Ichihara *et al.*, 1996) and grating-based (Neil *et al.*, 1997) structured illumination systems. Such programmability allows not only the adaptation of the illumination to a particular experiment (objective magnification and NA, sample thickness), but also dynamic adjustment in response to changes in the local structure of the specimen.

Here, we demonstrate the use of this feature for implementing the concept of controlled light exposure microscopy (CLEM; Hoebe *et al.*, 2007, 2008) in the PAM. Regions of the sample devoid of signal (background) or containing bright structures are exposed to less light by local modulation of the illumination. Optical sectioning is still achieved and rapid changes in cellular structure or position can be followed in live-cell imaging performed over prolonged periods of time.

Controlled light exposure microscopy

Unless multiphoton illumination is employed, the volume of excitation in a confocal microscope is not restricted to the plane of focus but spreads out in a biconical distribution. Thus, depending on the distribution of emitting species in the sample, most of the illumination may elicit fluorescence from out-of-focus objects, signals which are rejected by the pinhole located in front of the detector (Fig. 1). To the extent that a given object lies in the illumination cones of many neighbouring

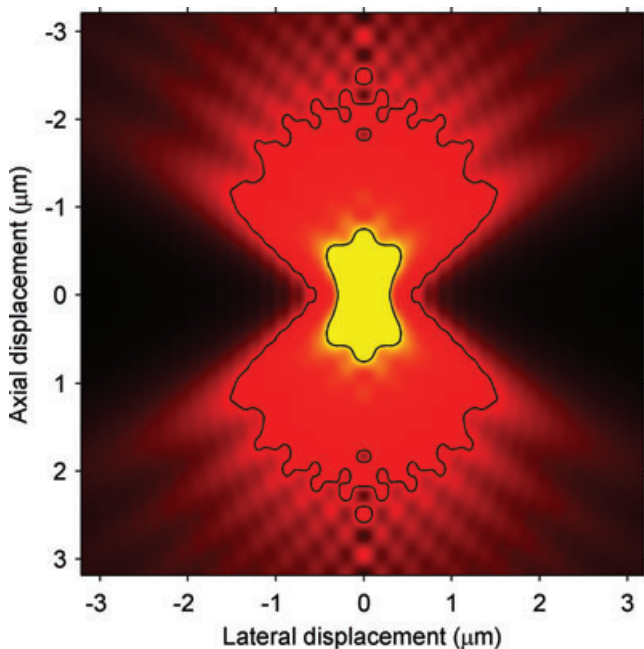


Fig. 1. Comparison of 488 nm excitation (outer contour) and confocal detection (inner contour) point spread functions for a 1.45 NA objective. Note that much of the sample above, below, and to the side of the detected point is also illuminated. Image is contrast-stretched for clarity.

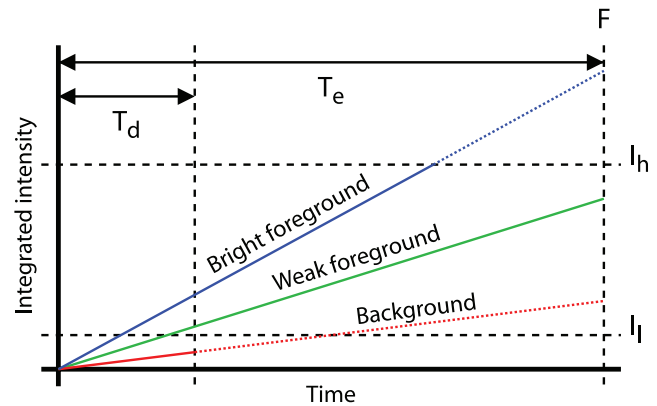


Fig. 2. CLEM in a scanning system. Illumination is shut off when the integrated intensity after the decision time T_d is below I_l , or when it exceeds I_h . In all cases, the intensity is extrapolated to the pixel dwell or exposure time T_e .

pixels, this effect can be quite dramatic. In addition, brightly fluorescent in-focus objects receive the same illumination dose as weakly fluorescent ones, even though an adequate SNR could be achieved with less illumination. Controlled light exposure microscopy (Hoebe *et al.*, 2007, 2008) dynamically readjusts the illumination during acquisition to minimize photobleaching. The out-of-focus fluorophores thus remain available for signal generation after subsequent displacement of the z -axis, repositioning them into the focal plane.

CLEM has been implemented in a CLSM such as the Nikon C1 and A1 (Balzar, 2007) by introducing a fast shutter into the optical path of the illuminating laser (Fig. 2). After exposing a pixel for a fraction T_d of the pixel dwell or exposure time T_e (called the decision time), the pixel is classified as either foreground or background. That is, if the integrated intensity after the decision time is below a threshold I_l , the pixel is considered to be uninteresting background and the illumination is shut off for the rest of T_e . If the intensity is higher than I_l , the pixel is assigned to the foreground, and exposure continues until a second signal threshold I_h is reached, at which time the light is also interrupted. At this bright foreground level, the SNR is adequate such that further improvement is not required. If the I_h level is not reached, illumination continues until the end of T_e . In all cases, the signal is divided by the actual illumination time T_{ill} so as to extrapolate linearly to the value that would be achieved under normal (constant) illumination, albeit in the absence of photobleaching or other photoconversion processes. The resulting image can then be further processed in the same manner as in conventional acquisition (De Vos *et al.*, 2009).

The programmable array microscope

The single-point scanning nature of CLSMs imposes practical and fundamental limits on the achievable speed of image

acquisition. The galvanometers that are employed in such systems are incapable of generating video rate two-dimensional images at 512×512 sampling points, and have the very low illumination duty cycle of $1/N$ (where N is the number of pixels). Furthermore, conventional photomultiplier detectors have relatively low quantum efficiencies compared to charge-coupled device sensors. More fundamentally, the high light intensities needed for fast single-point scanning can readily lead to fluorophore saturation (Visscher *et al.*, 1994) and other nonlinear photophysical processes (Beutler *et al.*, 2009). Multipoint (Petran *et al.*, 1968; Ichihara *et al.*, 1996) or line (Sheppard & Mao, 1988; Wolleschensky *et al.*, 2006) scanning and structured illumination (Neil *et al.*, 1997) techniques alleviate these concerns by distributing the illumination intensity over a larger part of the sample, thereby increasing the duty cycle by orders of magnitude.

The PAM (Verveer *et al.*, 1998; Hanley *et al.*, 1999; Heintzmann *et al.*, 2001; Hagen *et al.*, 2007), a member of the programmable structured illumination family of instruments (Liang *et al.*, 1997), is unique in providing dynamically adjustable pixel-by-pixel control of the local excitation intensity (or more generally, dose), and is thus very suitable for implementing the CLEM strategy in a widefield microscope system. The PAM incorporates a SLM in an image plane to create a pattern of conjugate illumination and detection. Only the selected 'on' SLM elements (leading to a specified deviation of the excitation light by specular reflection or to rotation of polarization) illuminate the sample according to a distribution dictated by the microscope objective. The fluorescence emitted by fluorophores located in the focal plane is received by the same elements and is recorded by a digital camera as a 'conjugate' image, F_c . Fluorescence originating from out-of-focus fluorophores impinges mainly on 'off' elements of the SLM and is recorded as a parallel 'nonconjugate' image, F_{nc} , generally with the same detector. An optically sectioned image is then generated in real time by scaled subtraction at each pixel position: $F_{os} = F_c - \alpha F_{nc}$, where the scaling factor $\alpha = d/(1-d)$ is related to the duty cycle d (Heintzmann *et al.*, 2001). The pattern is scanned over the sample during the exposure (typically in 24 steps in the case of the LCoS-based PAM; Hagen *et al.*, 2007, 2009) such as to cover the entire field while maintaining the given duty cycle for all pixels. Patterns range from dot scans (equivalent to Nipkow spinning disk systems) to line scans and one- or two-dimensional pseudorandom (Sylvester) sequences (Juskaitis *et al.*, 1996; Wilson *et al.*, 1996; Hanley *et al.*, 1999; Heintzmann *et al.*, 2001). The latter patterns can achieve a duty cycle of up to 50%, resulting in very rapid operation.

In the PAM, one can define multiple, arbitrary regions of interest (ROI) by simply applying a mask to the pattern generated on the SLM. Unmasked areas display the scanning pattern, whereas masked areas are always 'off'. The masks can be updated quickly and dynamically, making the PAM particularly suitable for implementing photobleaching

reduction by exposure control, ROI tracking and other dynamic sample-dependent techniques (Hagen *et al.*, 2009). We note that spatial, including angular, control over local illumination has also been achieved in light field microscopy by combining SLMs and microlens elements (Levoy *et al.*, 2009). However, such systems do not yet feature optical sectioning.

Minimizing light exposure with the PAM

As exposure control is already an inherent feature of the PAM, we denote our technique minimized light exposure-PAM (MLE-PAM). The principle is straightforward. For each slice, an initial unmasked subframe F_1 is taken with an exposure time T_d , and an illumination schedule is constructed. This schedule specifies the illumination time T_{ill} for each pixel p in the image, and is determined by predicting the time it would take the pixel to reach a given value I_h , assuming a linear response. Background pixels, with intensities $F_1(p) < I_l$, are masked out.

$$T_{ill}(p) = \begin{cases} T_d \frac{I_h}{F_1(p)} & \text{if } I_l < F_1(p) < I_h, \\ T_d & \text{otherwise.} \end{cases} \quad (1)$$

Next a series of $N - 1$ subframes is taken, each with an exposure time T_d . In the illumination pattern corresponding to subframe F_n , elements assigned a $T_{ill} \leq (n - 1)T_d$ are masked out. That is, the actual exposure time for each pixel is a discrete value and a multiple of the single frame exposure time T_d (Fig. 3). The maximum exposure time is limited to NT_d .

$$T_{ill,disc}(p) = \min\left(\left\lceil \frac{T_{ill}(p)}{T_d} \right\rceil, N\right) \cdot T_d \quad (2)$$

Finally, the subframes are summed and divided by the discretized exposure time for each pixel, creating the resulting image F_{res} . To reduce noise, nonilluminated parts of the subframes are excluded during summation, because they

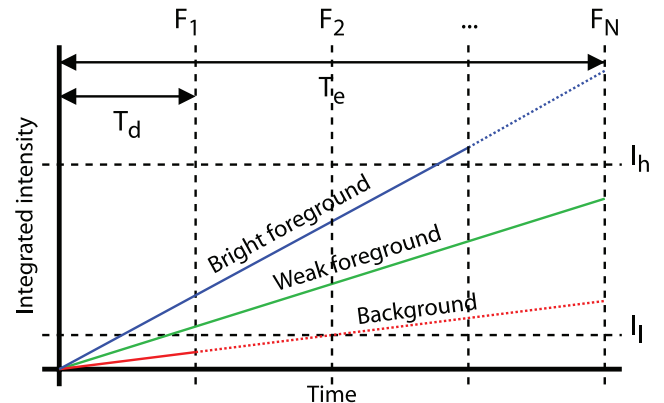


Fig. 3. MLE-PAM is a frame-wide discretized version of CLEM in a scanning system. The decision to turn off illumination is taken for all pixels at the same time, at static intervals (multiples of the frame time T_d).

contribute only to the noise, not to the signal.

$$F_{\text{sum}}(p) = \sum_{n=1}^N \begin{cases} F_n(p) & \text{if } T_{\text{ill,disc}}(p) \geq nT_d, \\ 0 & \text{otherwise,} \end{cases} \quad (3)$$

$$F_{\text{res}}(p) = \frac{F_{\text{sum}}(p)}{T_{\text{ill,disc}}(p)}. \quad (4)$$

The PAM is a widefield system – albeit with optical sectioning properties – such that changing the illumination of a given spot affects the measured brightness of its neighbouring pixels in accordance with the objective's point spread function (PSF), thereby leading to potential border artefacts. Although a point scanning system has a similar PSF, the illumination of an isolated point does not affect its neighbours because they are illuminated and detected sequentially.

Because of the spatial correlation between neighbouring points, the degree of which depends on the structure of the sample, it is not generally possible to reconstruct an image based solely on the illumination map T_{ill} and subframes F_1, \dots, F_N . We therefore extend (dilate) the illumination for each subframe F_n by the width of the point spread function in pixels d_{psf} , thereby fulfilling the condition that the contributions of the neighbours remain equal. As a consequence, the actual illumination exceeds somewhat the limit of 'useful' illumination. Only pixels that are more than d_{psf} pixels away from the illumination mask border can be used

for reconstruction.

$$T_{\text{ill,actual}}(p) = \text{Dilation}(T_{\text{ill,disc}}(p), d_{\text{psf}}), \quad (5)$$

$$T_{\text{ill,useful}}(p) = \text{Erosion}(T_{\text{ill,actual}}(p), d_{\text{psf}}), \quad (6)$$

$$F'_{\text{sum}} = \sum_{n=1}^N \begin{cases} F_n(p) & \text{if } T_{\text{ill,useful}}(p) \geq nT_d, \\ 0 & \text{otherwise,} \end{cases} \quad (7)$$

$$F'_{\text{res}}(p) = \frac{F'_{\text{sum}}(p)}{T_{\text{ill,useful}}(p)}. \quad (8)$$

For the reconstruction algorithm, we make use of the fact that as in the case of other optically sectioning microscopes, the detection PSF of the PAM is limited in extent (Hell & Schönle 2006). In a pure widefield microscope this is not the case, such that the application of sophisticated deconvolution techniques is required for reconstruction. Figure 4 shows the different stages in the MLE-PAM illumination and reconstruction scheme. Note that the SNR in the background of the reconstructed image in Fig. 4(b) is worse than in the non-MLE-PAM image (panel a), whereas it is the same in the foreground. Reduced SNR in the bright foreground (where illumination is also reduced) is hard to perceive, and if I_h is chosen carefully it will not have an influence on further analysis. If the camera gain is calibrated to yield photon counts (van Vliet *et al.*, 1998), the threshold can be directly derived from the required SNR.

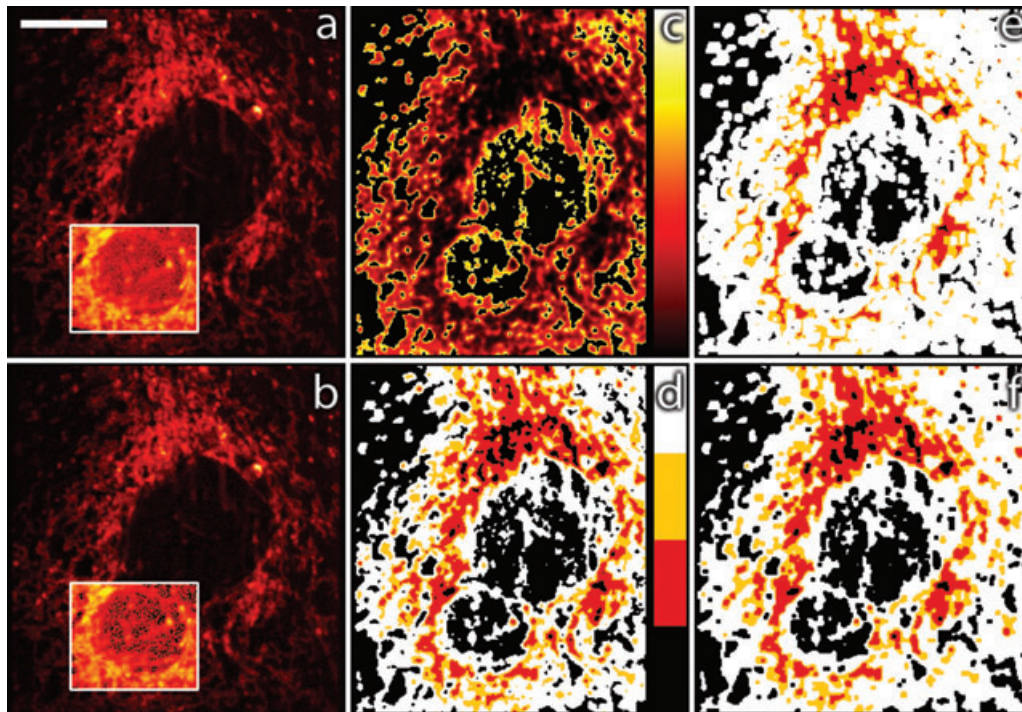


Fig. 4. Different stages in MLE-PAM illumination and reconstruction. Marsupial cell stained with Rhodamine 123 to visualize mitochondria. Scale bar 10 μm . (a) Non-MLE-PAM image. (b) Reconstructed image (F'_{res}). (c) Required illumination to reach I_h (T_{ill}). (d) Discretized illumination ($T_{\text{ill,disc}}$). (e) Actual illumination ($T_{\text{ill,actual}}$). (f) Useful illumination ($T_{\text{ill,useful}}$). The highlighted areas are contrast-stretched to enhance the visibility of the background noise.

Improvements provided by MLE-PAM

1. A major advantage of making the foreground/background decision for all pixels simultaneously instead of individually is that the spatial relationship between them can be taken into account. In scanning CLEM, noise within the decision time can lead to the incorrect classification of a pixel as background. Because the extrapolated intensity is then always an underestimation, it leads to a 'black hole' artefact at that pixel. Although the previously scanned neighbourhood could be used, this has not been implemented in practice except by simulation (Hoebe, 2009). In MLE-PAM, filtering T_{ill} to reduce noise before making the foreground/background decision is trivial, and we use both Gaussian filtering on the decision subframe F_1 as well as morphological filtering on the discretized illumination image $T_{\text{ill,disc}}$ (these filters are not applied during reconstruction, and therefore do not affect the resolution of the final image). As a result, the minimum background decision time (relative to the total exposure time) for avoiding artefacts due to misclassification is lower than in scanning CLEM. Furthermore, the background threshold can be determined dynamically via automatic background detection.
2. CLEM is typically applied not to two-dimensional images, but rather to a time series of three-dimensional images. All pixels in these images are illuminated for at least T_d . Assuming that the foreground/background decision only changes near the interface, we can reduce the illumination even further by not illuminating the pixels beyond this interface at all. In MLE-PAM, we have implemented this by introducing a third threshold, $I_u < I_l$, below which pixels will not even be illuminated for T_d at the next point in the time series. In essence, this creates an ROI around the sample foreground. Of course, the consequence is that changes in intensity outside of the ROI will not be registered. It is therefore imperative to compensate for sample motion by applying a 3D dilation to the segmented ROI, scaled according to the maximum expected distance travelled between frames. For fast moving samples, this creates a 'lagging spotlight' effect, according to which the sample seems to 'push' the illumination (Fig. 5). If the motion is regular, it is also possible to decrease the amount of dilation by predicting the position of the sample in the next frame.
3. The effectiveness of any CLEM procedure depends on the structure of the sample. Samples occupying only a small volume fraction of the field of view benefit more than uniform ones. For tracking studies it can therefore be advantageous to combine MLE-PAM with the targeted activation of parts of the sample using a photoconvertible dye. In our implementation of this scheme, all fluorophores in the sample are first dimly photoactivated using a 405 nm laser, after which a segmentation algorithm determines which subset will be tracked. By illuminating these parts

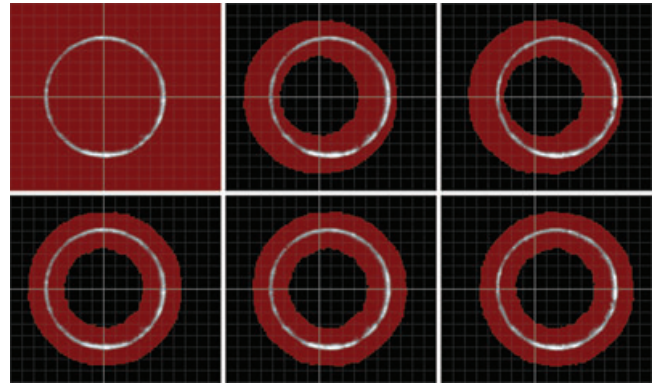


Fig. 5. ROI tracking of a moving 6 μm surface-stained bead sample by MLE-PAM. The red region in the top row is the illumination applied to acquire the image, while the bottom row shows the illumination that is calculated from that image, which is the same as the illumination applied to the next image. Scanning the sample using a stage results in the bead 'pushing' the illumination to the right. The crossed lines indicate the starting position of the bead.

for a longer period, they are activated fully, after which the regular MLE-PAM time-series acquisition is carried out at 488 nm excitation. If longer tracking is necessary, it is possible to activate a new subset of molecules and continue the measurement.

Experimental procedures

Measurements were conducted on a lab-constructed Gen2-LCoS PAM (Hagen *et al.*, 2007, 2009) attached to an Olympus IX71 microscope (Olympus, Hamburg, Germany) and equipped with an Andor iXon DV897 back-thinned EMCCD camera (Andor Technology PLC, Belfast, Northern Ireland). Excitation was with a Coherent Innova90 Argon-Ion laser (Coherent, Inc., Santa Clara, CA U.S.A.) operated at 488 nm, with an 'on-time' irradiance in the focal plane of $\sim 10 \text{ W cm}^{-2}$. The CLEM background decision time was 25% of the total illumination time ($T_c = 4T_d = 67 \text{ ms}$), and illumination was extended by 180 nm laterally ($d_{\text{psf}} = 3$ pixels). Sample motion compensation added another 310 nm laterally and an axial dilation of one slice for the first subframe.

Photobleaching measurements were performed on HeLa cells, in which the mitochondria were stained with Invitrogen mitotracker FM green (Life Technologies, Carlsbad, CA, U.S.A.). Cells were incubated for 20 min with a 0.2 μM dye solution in RAB/BSA (0.5 mg mL^{-1} BSA in Tyrode's buffer: 135 mM NaCl, 10 mM KCl, 0.4 mM MgCl_2 , 1 mM CaCl_2 , 5.6 mM glucose, 10 mM HEPES, pH 7.2), then washed and immersed in RAB/BSA. Using an Olympus 150 \times 1.45 NA oil immersion objective, two fields of ten 1 μm slices were measured in an interleaved fashion with a Prior H1P7 motorized XY stage (Prior Scientific Inc., Rockland, MA, U.S.A.). One field used MLE-PAM illumination, while

the other served as a control with full-field illumination at the weak foreground level.

We also imaged the distribution of polyhomeotic GFP (PhGFP; Netter *et al.*, 2001) in *Drosophila* imaginal disks, using a single field. In this case, the MLE-PAM masks were applied only to the top half of the image, while the bottom half was exposed to constant illumination. Bleaching curves were calculated by tracking and averaging the intensity of three loci in both halves using View5D (R. Heintzmann, King's College London, London, U.K.). For these samples, 20 slices with 500 nm separation were taken.

The photoactivation experiments were performed on *Drosophila* embryos in which the H2AvD histone was tagged with paGFP (Patterson & Lippincott-Schwartz 2002), using an Olympus 40 \times 1.15 NA water objective. The activation wavelength was 405 nm, provided by a Blue Sky FMOD405 diode laser (Blue Sky Research, Milpitas, CA, U.S.A.). The Z stacks consisted of 10 slices with 2 μ m separation.

Online real-time MLE-PAM calculations were executed on a GeForce 8800GTX graphics card (NVIDIA Corporation, Santa Clara, CA, U.S.A.) using CUDA (Nickolls *et al.*, 2008). Offline image analysis was performed in MATLAB (The MathWorks, Inc., Natick, MA, U.S.A.) using the DIPimage toolbox (Delft University of Technology, Delft, The Netherlands).

Further results and discussion

We verified the decreased photobleaching achieved with MLE-PAM using HeLa cells stained with a live cell mitochondria marker. Figure 6 and Movie S1 show the maximum intensity

projection over ten 1 μ m slices for four time points of both normally illuminated and MLE-PAM-illuminated cells. The MLE-PAM sample required a 2.5-fold longer exposure time to photobleach half the initial fluorescence compared to normal illumination. The calculation was based on the mean fluorescence intensity over background and corresponded well with the light dose to the specimen, which in this experiment was reduced by a factor of 2.7. The overall light dose reduction was 5.8-fold, but much of that was in the background, which did not photobleach. This value was computed by simulating the light field inside the sample using the applied masks and the objective PSF, and integrating either over the entire field or just the foreground voxels, a procedure similar to that used in the calculation of the CLEM factor (Hoebe *et al.*, 2008).

We also imaged the PhGFP distribution in *Drosophila* imaginal disks (Ficz *et al.*, 2005). Figure 7 shows the average intensity of three PhGFP loci for both the MLE-PAM processed and normally illuminated part of a sample. According to the exponential fits, there was a 4.7 \times reduction in the photobleaching rate constant, showing that sparse samples can experience a much larger reduction in light dose than more uniform samples (see also Fig. 8 and Movie S2). However, the latter can still benefit from MLE-PAM if one is only interested in a sparse subset (region).

For example, in the examination of the movement of cells in a *Drosophila* embryo, it is not necessary to follow all the cells; indeed, this can complicate the tracking if there is too much overlap. By labelling the cells with a photoconvertible dye and activating only a sparse subset, the sample could be imaged

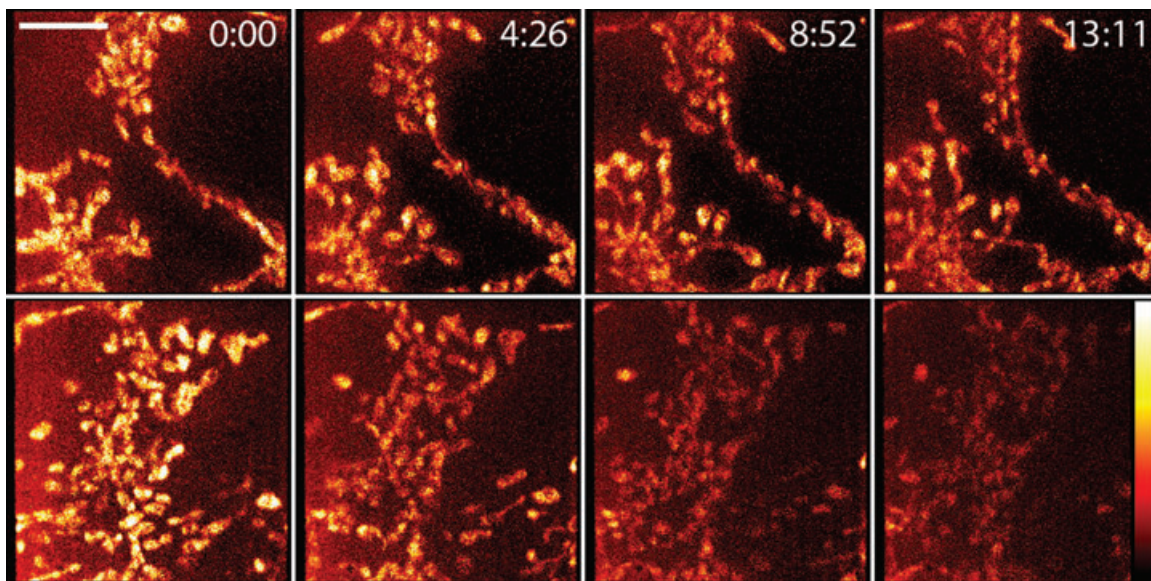


Fig. 6. Comparison of photobleaching using normal illumination and MLE illumination in the PAM. Images are maximum intensity projections over ten 1 μ m slices of a HeLa cell stained with mitotracker to visualize mitochondria. Top row is MLE, bottom row normal PAM imaging. Images were taken under the same conditions in an interleaved fashion using an automated XY stage. Scale bar 5 μ m. See also Movie S1.

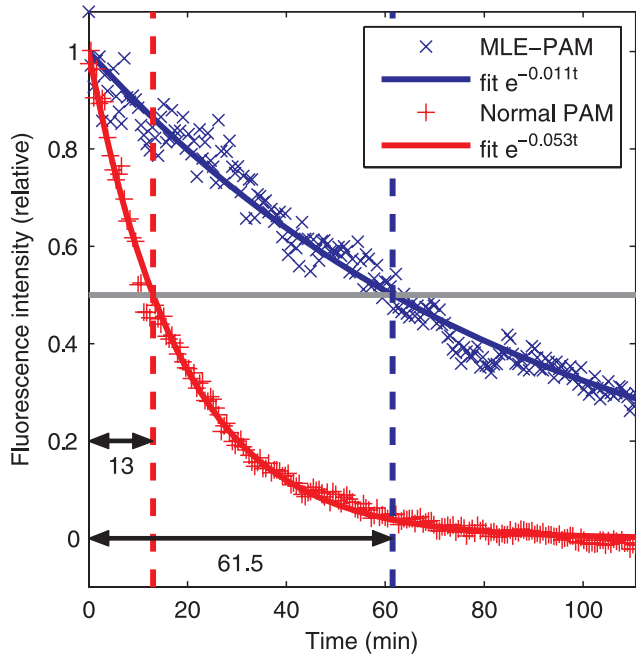


Fig. 7. Time course of photobleaching and exponential fits from images of the distribution of PhGFP in *Drosophila* imaginal disks. Curves show the average intensity above background of three tracked loci in the MLE-PAM (top panel) and normal (bottom panel) halves of a single field.

over a much longer period of time by using MLE-PAM. In an experiment with *Drosophila* embryos in which the H2AvD histone was tagged with paGFP and a single cell was tracked, a reduction in the foreground light dose by a factor of 4.1 was

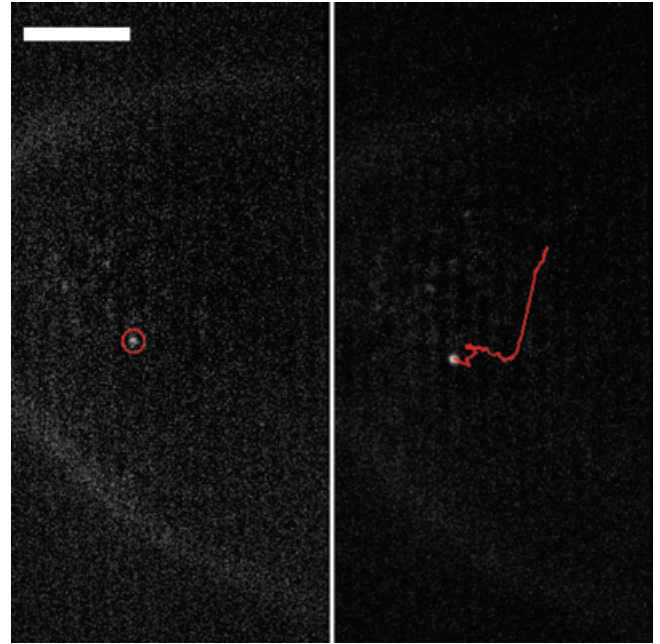


Fig. 9. Activation and tracking of a paGFP-tagged H2AvD expressing cell in a *Drosophila* embryo. (Left panel) Image after initial 16 ms photoactivation and overlaid automatically segmented activation site. (Right panel) Image after 2 s selective activation including subsequent particle track over 20 min. Scale bar 20 μm . See also Movie S3.

achieved (Fig. 9 and Movie S3). If photobleaching is still too rapid in such an experiment, rendering the activated subset too dim for tracking, one can subsequently activate and track a new subset.

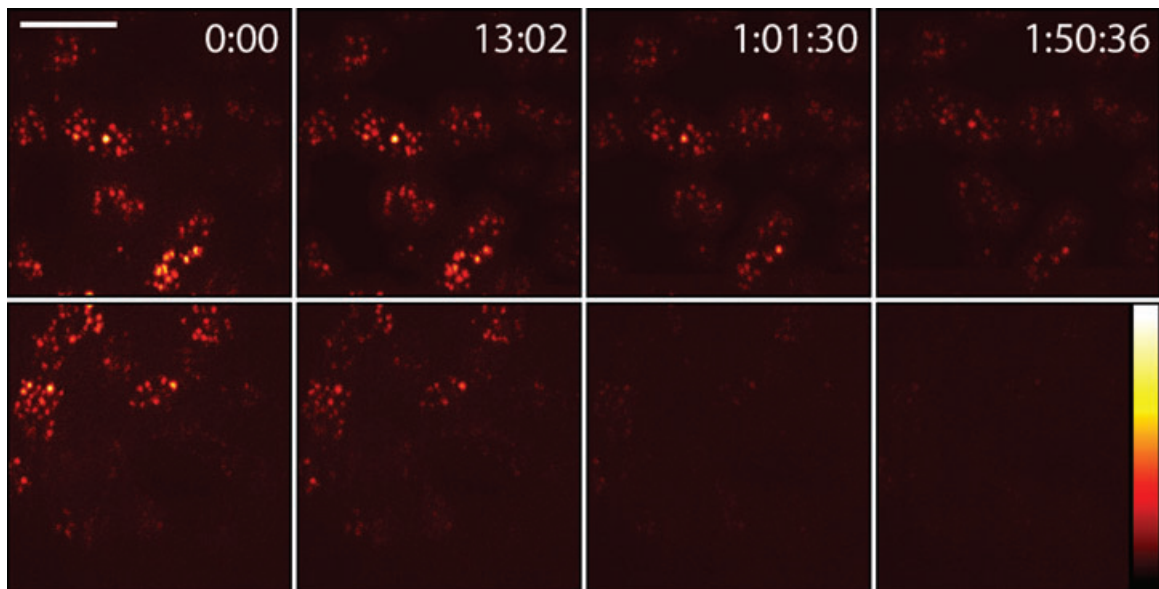


Fig. 8. MLE-PAM (top panel) and normal (bottom panel) images at different time points of the PhGFP bleaching curves in Fig. 7. The time points correspond to the start, normal half-life, MLE-PAM half-life and end of the acquisition, respectively. MLE-PAM and normally illuminated images were captured side-by-side in the same field. Maximum intensity projections over 20 $0.5 \mu\text{m}$ slices. Scale bar 5 μm . See also Movie S2.

MLE-PAM can operate using a lower background decision time than regular scanning CLEM because the decision subframe F_1 can be filtered. In simulation, we compared the foreground of the image in Fig. 4(a) to the same area in the reconstructed image (panel b) and a reconstruction without filtering. With equal thresholds, the unfiltered reconstruction required a 3-fold longer decision time to reach the same mean squared error as the filtered decision. Even when the threshold was adjusted to achieve the same amount of foreground pixels for both strategies, the difference was still more than a factor of two.

An interesting side effect of using a low background decision time is that the SNR in the background is very low. The MLE-PAM technique assumes that such regions of the image are not of interest. However, they affect the maximum intensity projection inasmuch as the background noise in one slice corrupts the foreground of other slices. For maximum intensity projections, therefore, we filtered the background with a uniform filter in the time domain, such that the final SNR was equal to that which would have been achieved using full illumination. The resulting reduction in temporal resolution of the background was of no consequence because such areas are devoid of information.

Compared to scanning CLEM, MLE-PAM yields a slightly lower intrinsic light reduction factor because of the dilated illumination, the effect of which depends on the structure of the sample. Considering samples with equal total foreground volume, CLEM has the greatest effect in the case of small uniformly distributed spots, as can be easily perceived in Fig. 1: a voxel is most brightly illuminated when either itself or its neighbours (especially in Z) are sampled. Thus, reducing the illumination of a voxel's neighbours has more of an influence than a reduction somewhere else. It follows that CLEM is most effective in samples in which the foreground pixels are surrounded by background (as in a uniform spotty distribution) and less when the foreground is clustered in a single area.

We quantified this effect by calculating the mean distance to foreground across a series of simulated test images with increasing spot size but equal foreground volume (Fig. 10). The mean distance to foreground is defined by averaging the Euclidean distance (in voxels) of each voxel to the nearest foreground voxel over all voxels in the image. The simulation used the same parameters as our experiments: 62 nm pixel size and a 1.45 NA oil objective with 488 nm excitation. Two sets of lines are shown, for two different fractional foregrounds roughly corresponding to the experiments in Figs 6 (10%) and 8 (3%). The top lines of the two sets indicate regular (no dilation) CLEM imaging, although with a zero background decision time. The illumination reduction factor decreases for increased spot size. In MLE-PAM, however, the illumination is dilated to remove border artefacts, a process that has a larger negative effect in samples with small uniformly distributed spots.

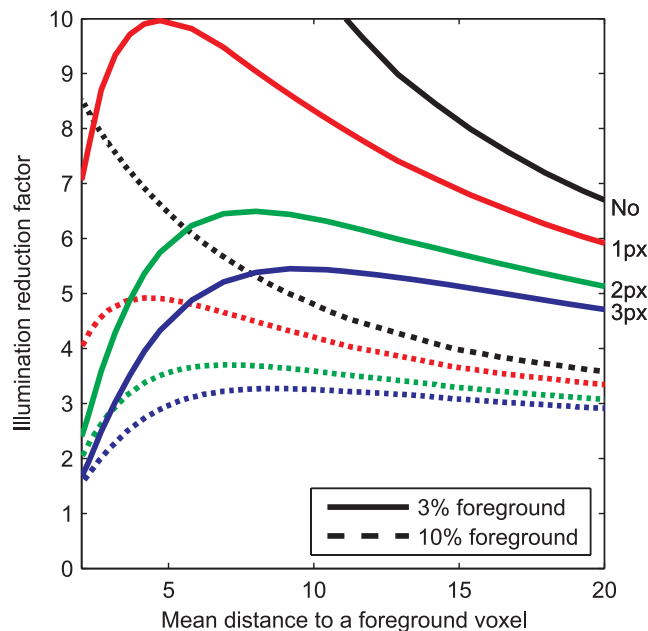


Fig. 10. Simulation of the effect of dilated exposure ROI on reduction of foreground illumination. Larger dilations (shown in pixel units) reduce the illumination reduction factor, especially in samples consisting of small uniformly distributed spots (left end of the graph). The difference (but also the general illumination reduction) is smaller for more clustered samples (right end of the graph).

As can be seen in the lower lines of Fig. 10, an optimum exists for the distribution of the sample most favourable for MLE-PAM. For our experimental parameters (d_{psf} of 3 pixels), this optimum lies between 5 and 10 voxels mean distance to foreground; our samples exhibited values of 9–12. As can be judged from the relative flatness of the lines representing larger dilations in this region, the benefits of MLE-PAM derive more from the overall reduction of light dose due to a low fraction of the sample being illuminated than from switching off the illumination in immediately neighbouring voxels.

This report has dealt with the relative performance of MLE-PAM and regular PAM imaging. Compared to a conventional widefield microscope, the PAM has a somewhat reduced light throughput due to the less than ideal reflectivity of the SLM (only 60% of the light impinging on the 'on' pixels reaches the conjugate image). On the other hand, optical sectioning by widefield acquisition + deconvolution typically requires narrowly spaced sampling in the Z-axis, leading to long acquisition times and a corresponding signal loss.

Conclusions

We have demonstrated that controlled light exposure microscopy can be implemented in the PAM (MLE-PAM), by simply masking the SLM. Border artefacts at the edges

of the masks are avoided by dilating the illumination with respect to the used image regions based on the width of the PSF. Furthermore, we extended the minimized exposure into the time domain, automatically creating ROIs around the foreground pixels while taking care to compensate for sample movement. Finally, we showed that MLE-PAM may be combined with targeted photoactivation to reduce photobleaching in tracking studies. These improvements render the PAM even more useful for extended live cell imaging.

Acknowledgements

The authors thank Ron Hoebe (Academic Medical Center, University of Amsterdam) and Erik Manders (Swammerdam Institute for Life Sciences, University of Amsterdam) for useful discussions. This work was supported by the EU 6th framework (FP6) project FLUOROMAG, LHSB-CT-2006-037465.

References

- Balzar, M. (2007) Controlled light exposure microscopy. *Imaging Microsc.* **9**(4), 68–69.
- Beutler, M., Hinck, S. & de Beer, D. (2009) A method for imaging of low pH in live cells based on excited state saturation. *J. Microbiol. Methods* **77**, 98–101.
- Bruchez, M., Moronne, M., Gin, P., Weiss, S. & Alivisatos, A.P. (1998) Semiconductor nanocrystals as fluorescent biological labels. *Science* **281**, 2013–2016.
- De Vos, W.H., Hoebe, R.A., Joss, G.H., Haffmans, W., Baatout, S., Van Oostveldt, P. & Manders, E.M.M. (2009) Controlled light exposure microscopy reveals dynamic telomere microterritories throughout the cell cycle. *Cytometry A* **75A**, 428–439.
- Ficz, G., Heintzmann, R. & Arndt-Jovin, D.J. (2005) Polycomb group protein complexes exchange rapidly in living drosophila. *Development* **132**, 3963–3976.
- Hagen, G.M., Caarls, W., Thomas, M., *et al.* (2007) Biological applications of an LCoS-based programmable array microscope (PAM). *Imaging, Manipulation, and Analysis of Biomolecules, Cells, and Tissues V (Proc. Photonic West 2007, BiOS)* (eds. by D.L. Farkas, R.C. Leif & D.V. Nicolau), vol. 6441, pp 64410S. SPIE.
- Hagen, G.M., Caarls, W., Lidke, K.A., De Vries, A.H.B., Fritsch, C., Barisas, B.G., Arndt-Jovin, D.J. & Jovin, T.M. (2009) Fluorescence recovery after photobleaching and photoconversion in multiple arbitrary regions of interest using a programmable array microscope. *Microsc. Res. Technol.* **72**, 431–440.
- Hanley, Q.S., Verveer, P.J., Gemkow, M.J., Arndt-Jovin, D.J. & Jovin, T.M. (1999) An optical sectioning programmable array microscope implemented with a digital micromirror device. *J. Microsc.* **196**, 317–331.
- Heintzmann, R., Hanley, Q.S., Arndt-Jovin, D. & Jovin, T.M. (2001) A dual path programmable array microscope (PAM): simultaneous acquisition of conjugate and non-conjugate images. *J. Microsc.* **204**, 119–135.
- Hell, S.W. & Schönle, A. (2006) Nanoscopy: The future of optical microscopy. *Biomedical Optical Imaging* (eds. by Fujimoto, J.G. & D.L. Farkas), pp. 237–263. Oxford University Press, Oxford.
- Hoebe, R. (2009) *Controlled Light Exposure Microscopy*. PhD thesis, Universiteit van Amsterdam.
- Hoebe, R.A., Van Oven, C.H., Gadella, T.W.J., Dhonukshe, P.B., Van Noorden, C.J.F. & Manders, E.M.M. (2007) Controlled light-exposure microscopy reduces photobleaching and phototoxicity in fluorescence live-cell imaging. *Nat. Biotechnol.* **25**, 249–253.
- Hoebe, R.A., Van Der Voort, H.T.M., Stap, J., Van Noorden, C.J.F. & Manders, E.M.M. (2008) Quantitative determination of the reduction of phototoxicity and photobleaching by controlled light exposure microscopy. *J. Microsc.* **231**, 9–20.
- Ichihara, A., Tanaami, T., Isozaki, K., Sugiyama, Y., Kosugi, Y., Mikuriya, K., Abe, M. & Uemura, I. (1996) High-speed confocal fluorescence microscopy using a nipkow scanner with microlenses for 3D-imaging of single fluorescent molecule in real time. *Bioimages* **4**, 57–62.
- Juskaitis, R., Wilson, T., Neil, M.A.A. & Kozubek, M. (1996) Efficient real-time confocal microscopy with white light sources. *Nature* **383**, 804–806.
- Levoy, M., Zhang, Z. & McDowall, I. (2009) Recording and controlling the 4D light field in a microscope using microlens arrays. *J. Microsc.* **235**, 144–162.
- Liang, M., Stehr, R.L. & Krause, A.W. (1997) Confocal pattern period in multiple-aperture confocal imaging systems with coherent illumination. *Opt. Lett.* **22**, 751–753.
- Lidke, D.S. & Arndt-Jovin, D.J. (2004) Imaging takes a quantum leap. *Physiology* **19**, 322–325.
- Neil, M.A.A., Juskaitis, R. & Wilson, T. (1997) Method of obtaining optical sectioning by using structured light in a conventional microscope. *Opt. Lett.* **22**, 1905–1907.
- Netter, S., Faucheux, M. & Théodore, L. (2001) Developmental dynamics of a polyhomeotic-EGFP fusion in vivo. *DNA Cell Biol.* **20**, 483–492.
- Nickolls, J., Buck, I., Garland, M. & Skadron, K. (2008) Scalable parallel programming with CUDA. *ACM Queue* **6**, 40–53.
- Patterson, G.H. & Lippincott-Schwartz, J. (2002) A photoactivatable GFP for selective photolabeling of proteins and cells. *Science* **297**, 1873–1877.
- Petran, M., Hadravsky, M., Egger, M.D. & Galambos, R., (1968) Tandem-scanning reflected-light microscope. *J. Opt. Soc. Am.* **58**, 661–664.
- Sheppard, C.J.R. & Mao, X.Q. (1988) Confocal microscopes with slit apertures. *J. Modern Opt.* **35**, 1169–1185.
- van Vliet, L.J., Sudar, D. & Young, I.T. (1998) Digital fluorescence imaging using cooled charge-coupled device array cameras. In *Cell Biology: A Laboratory Handbook, 2nd ed.*, vol. 3, pp. 109–120. Academic, London.
- Verveer, P.J., Hanley, Q.S., Verbeek, P., van Vliet, L.J. & Jovin, T.M. (1998) Theory of confocal fluorescence imaging in the programmable array microscope (PAM). *J. Microsc.* **189**, 192–198.
- Visscher, K., Brakenhoff, G.J. & Visser, T.D. (1994) Fluorescence saturation in confocal microscopy. *J. Microsc.* **175**, 162–165.
- Wilson, T., Juskaitis, R., Neil, M.A.A. & Kozubek, M. (1996) Confocal microscopy by aperture correlation. *Optics Lett.* **21**, 1879–1881.
- Wolleschensky, R., Zimmermann, B. & Kempe, M. (2006) High-speed confocal fluorescence imaging with a novel line scanning microscope. *J. Biomed. Opt.* **11**, 064011–1/14.

Supporting Information

Additional Supporting Information may be found in the online version of this article:

Movie S1: Comparison of photobleaching using normal and MLE illumination in the PAM. Images are maximum intensity projections over ten 1 μm slices of a HeLa cell stained with mitotracker to visualize mitochondria. Top row is MLE, bottom row normal PAM imaging. Images were taken under the same conditions in an interleaved fashion using an automated XY stage.

Movie S2: MLE–PAM (top) and normal (bottom) images at different time points of the PhGFP bleaching curves in Fig. 7. MLE–PAM and normally illuminated images were captured

side-by-side in the same field. Maximum intensity projections over twenty 0.5 μm slices.

Movie S3: Activation and tracking of a paGFP-tagged H2AvD expressing cell in a *Drosophila* embryo.

Please note: Wiley-Blackwell are not responsible for the content or functionality of any supporting materials supplied by the authors. Any queries (other than missing material) should be directed to the corresponding author for the article.